Applied Thermal Engineering 138 (2018) 122–132

Contents lists available at ScienceDirect

Applied Thermal Engineering

journal homepage: www.elsevier.com/locate/apthermeng

Research Paper

A multi-block lattice Boltzmann method for the thermal contact resistance at the interface of two solids

Wen-Zhen Fang, Jian-Jun Gou, Li Chen, Wen-Quan Tao*

Key Laboratory of Thermo-Fluid Science and Engineering, Ministry of Education, China
School of Energy & Power Engineering, Xi'an Jiaotong University, Shaanxi 710049, China

HIGHLIGHTS

- The contribution of gas conduction and radiation are properly considered.
- A multi-block lattice Boltzmann method is adopted to save computing resources.
- Influence factors on thermal contact resistance are systematically investigated.

ARTICLE INFO

Keywords:
Multi-block
Lattice Boltzmann method
Thermal contact resistance
Fractal

ABSTRACT

In the present paper, a patching type multi-block lattice Boltzmann method is adopted to predict the thermal contact resistance (TCR) at the interface of two solids. The rough surfaces of contact materials are reconstructed based on the fractal theory and the contact pressure is obtained based on the plastic deformation model. The accuracy of the patching type multi-block lattice Boltzmann method is validated by some benchmarks. After validations, effects of the contact pressure, roughness, thermal conductivity of contact material, thermal conductivity of interstitial medium, temperature and radiation on TCR are investigated. The results show that: the TCR decreases when the contact pressure increases, but increases with the root-mean-square roughness; the TCR of two contact aluminums decreases faster than that of stainless steels when contact pressure increases; a higher thermal conductivity of contact materials leads to a smaller TCR; when the thermal conductivity of interstitial medium is close to zero or the gap is in vacuum, the TCR is much larger than that filled with air, especially at low contact pressure; at the high temperature, the contribution of the radiation to the TCR becomes appreciable if the thermal conductivity of the interstitial medium is low. Especially when the gap is in vacuum, the contribution of radiation on the TCR cannot be neglected.

1. Introduction

Real surfaces (engineering surfaces) are not perfectly smooth and appear rough at the microscopic level. When two rough surfaces are brought into contact, only a few contact spots exist, resulting in a thermal contact resistance (TCR) at the interface when heat flux goes through it. TCR significantly effects the design and performance of the thermal engineering system and apparatus, such as spacecraft thermal protection systems and electronic devices. Many studies have been conducted on the prediction of interfacial TCR since 1950s. The approaches to determine the TCR can be divided into three categories: theoretical models, numerical models and experimental measurements. For theoretical models, the conforming rough surface contact conductance model [1] and the fractal prediction model [2–4] are the most famous ones. For numerical models, the finite element method (FEM) [5,6], finite difference method (FDM) [7] and lattice Boltzmann method (LBM) [8] were ever adopted to predict the TCR. As for experimental measurements, a reversible heat flux method [9] was performed to measure the TCR with high-precision instrumentations.

According to the published literatures, predictions of the TCR depends on three key issues: surface topography, deformation mechanisms and heat transfer calculations [6,10]. For the description of the surface topography, Greenwood and Williamson [11] found that the height profile of the rough surface approximately obeyed the Gaussian distribution, and later this finding was widely adopted in many TCR models until 1980s. In these Gaussian surface models, some statistical parameters, such as the root-mean-square roughness, absolute mean asperity slope and radius of curvature, are necessary to describe the

* Corresponding author at: Key Laboratory of Thermo-Fluid Science and Engineering, Ministry of Education, China.
E-mail address: wqtao@mail.xjtu.edu.cn (W.-Q. Tao).

https://doi.org/10.1016/j.applthermaleng.2018.03.095
Received 26 September 2017; Received in revised form 23 February 2018; Accepted 29 March 2018
Available online 30 March 2018
1359-4311/

rough surface. However, such parameters are heavily related to the precision and resolution of the measurement instrument, and there is no unique description for the rough surface profile due to the multiscale nature of rough surfaces [12]. Sayles and Thomas [13] found that variations of the height profile of rough surfaces possess a non-stationary random characteristic. Then, Majumdar and Tien [14] adopted some fractal parameters which are independent on the measurement scale to describe the surface topography, and a Weierstrass-Mandelbrot function based on the fractal theory has been widely adopted to generate rough surface profiles due to the self-similarity of surface roughness profile. For deformation mechanisms, three different types of deformation assumptions have been proposed: plastic [15,16], elastic [17] and elastoplastic [18] models. Tang et al. [19] used the FEM to investigate the surface roughness deformation characteristics of the reconstructed random surfaces. As for the heat transfer mechanism, there are three heat transport routes for the heat flux going through contact surfaces: (i) through the contact spots by conduction; (ii) across the air-filled gaps by conduction; (iii) by means of radiation between the non-contacted upper and lower surfaces. The convection at the micro-gaps can be totally neglected due to their small space sizes.

This paper focuses on the numerical prediction models of the TCR, especially in the heat transfer calculations. In this regard, several studies have been conducted. Murashov and Panin [5] adopted the FEM based on ANSYS software while Cui et al. [8] used a multiscale method by coupling LBM and FDM to predict the TCR, but they did not consider the contribution of gas conduction. Gou et al. [6] adopted the FEM to analyze the mechanical and thermal contact performance based on a practical rough surface topography measured by a contour profiler. Wahid [7] adopted the FDM to analyze heat conduction problem in a cylinder with a cone surface and found that the gas conduction is a significant part of TCR. Zhang et al. [15] developed an innovative grid system in the cylinder coordinate to predict the TCR considering gas conduction contributions. However, almost all the published papers neglected the contribution of the radiation to the TCR. To the authors' knowledge, only Yavanovich and Kitscha [20] provided a radiation resistance for the enclosure formed by the flat-sphere contact and its surrounding insulation, but it is an analytical model which is not suitable for complex surfaces. From the above brief review, it is obvious that developing a numerical model which can consider all heat transfer routes for prediction of TCR is highly needed.

The purpose of this paper is to develop a numerical method to predict the TCR considering the contribution of gas conduction and radiation. Fig. 1 schematically shows the TCR between two pieces of materials with rough surfaces. From the numerical point of view, the grid resolution in the contact regions shown by two dashed lines should be high enough while in the other two blocks of material 1 and 2 can be much coarser. Thus, a multi-block method is adopted to numerically

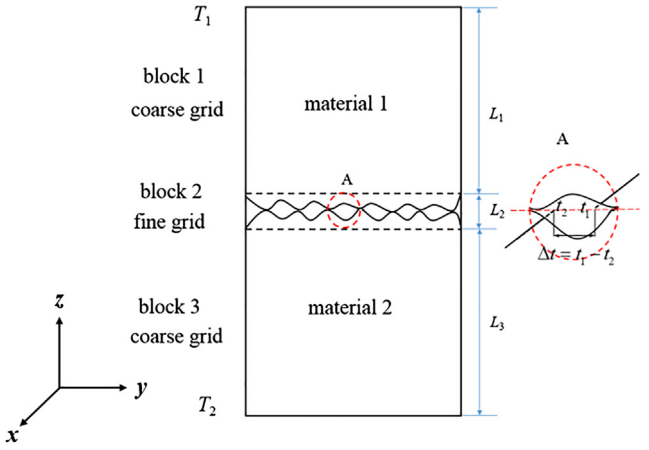

Fig. 1. Schematic diagram of thermal contact resistance.

predict the interfacial TCR. In the contact region, a fine grid system is needed to describe the surface with a sufficient resolution, while much coarser grid systems are chosen for two solid materials to save the computational resource and speed up the calculation time. For such domain decomposition method, the continuity of the physical quantities at the interface between the fine grid block and the coarse grid block should be ensured [21]. There exist two kinds of treatments to deal with the interfacial information exchange [21]. One is the overlapping type which has an overlapping region for the interfacial information exchange [21,22]. The other one is the patching type which only has a common layer shared by the two blocks [21,23]. Generally, the overlapping region method for the interfacial information exchange is more stable, however it requires the transport properties (thermal conductivity or viscosity) of different block are the same since there is an overlap region of two blocks. For predicting the TCR, the contact region is heterogeneous and the effective thermal conductivities of three blocks (shown in Fig. 1) are different. Therefore, in the present paper, we adopt the patching multi-block method to decompose the computational domain. The proposed multi-block method in Ref. [24] is only suitable for the case of which different blocks have the same physical properties. In the present paper, we extend this method to be suitable for the case of which different blocks can have different physical properties.

Lattice Boltzmann method (LBM) is an effective tool to solve the Navies-stokes equations and energy transport equation [25,26]. Due to its easy implementation for complex boundaries and parallel computation, LBM has been adopted to solve fluid flows in porous media [27] and to predict the effective thermal conductivity of heterogeneous materials with random microstructures [28,29]. In the predicting model of TCR, the entire computational domain is also heterogeneous since it contains an interstitial medium and two contact solid subdomains. Therefore, the LBM is suitable for predicting the TCR.

In the present paper, rough surfaces of contact materials are reconstructed based on the fractal theory and the contact pressure is obtained based on the plastic deformation model. A patching type multi-block parallel LBM using the OpenMP [30] is adopted to analyze the heat transfer in two contact materials. The rest of the present paper is organized as follows. First, the multi-block LBM for predicting the TCR is presented in Section 2. Two benchmarks are conducted in Section 3 to validate the accuracy of the present method. Then, effects of the contact pressure, roughness, thermal conductivity of the contact material, thermal conductivity of the interstitial medium, temperature and radiation on the TCR are discussed in Section 4. Finally, some conclusions are drawn in Section 5.

2. Numerical method

The computational domain for predicting the TCR at the interface is shown in Fig. 1. To numerically predict the TCR at the interface, we should solve the energy transport equation to obtain the heat flux and temperature drop at the interface. The energy transport equation for the entire computational domain can be expressed as:

$$\frac{\partial T}{\partial t} = \frac{\partial}{\partial x_i}\left(\frac{\lambda}{\rho c_P}\frac{\partial T}{\partial x_i}\right) + S \tag{1}$$

and its boundary conditions are:

$$T|_{z=l} = T_1; \quad T|_{z=0} = T_2; \quad \left.\frac{\partial T}{\partial x}\right|_{x=\partial\Omega} = 0 \tag{2}$$

where T is the temperature; λ is the thermal conductivity; ρc_p is the volumetric capacity; and S is the source term. If there is no any internal heat source, then $S = 0$. As for the radiative heat flux from the upper surface to lower surface, an additional heat source term is added at the nodes near the boundaries. The detailed implement of radiative heat source term will be discussed at Section 4.3.

2.1. Lattice Boltzmann method

In the LBM, the LB equation instead of the macroscopic energy transport equation shown in Eq. (1) should be solved. The LB equation for temperature distribution function can be expressed as [31]:

$$f_\alpha(\boldsymbol{x}+\boldsymbol{e}_\alpha\delta t,t+\delta t)-f_\alpha(\boldsymbol{x},t)=-\frac{1}{\tau}(f_\alpha(\boldsymbol{x},t)-f_\alpha^{eq}(\boldsymbol{x},t))+\delta t\omega_\alpha S \tag{3}$$

where $\boldsymbol{x}$ denotes the position, t is the real time, δt is the time step, f_i is the temperature distribution function, τ is the relaxation time, S is the source term and f_i^{eq} is the equilibrium temperature distribution function, defined as (D3Q7 model) [32]:

$$f_\alpha^{eq}=\omega_\alpha T,\alpha=0-6 \tag{4}$$

where $\omega_\alpha=1/7$. $\boldsymbol{e}_\alpha$ is the discrete velocity:

$$\boldsymbol{e}_\alpha=\begin{bmatrix}0&1&-1&0&0&0&0\\0&0&0&1&-1&0&0\\0&0&0&0&0&1&-1\end{bmatrix}c \tag{5}$$

The relation between the macroscopic thermal diffusivity (a) and the relaxation time coefficient (τ) can be obtained by Chapman-Enskog expansion (see Appendix A):

$$a=\frac{2}{7}c^2\left(\tau-\frac{1}{2}\right)\delta t \tag{6}$$

The local temperature can be obtained by:

$$T=\sum_\alpha f_\alpha \tag{7}$$

and the local heat flux along z direction can be calculated by (see Appendix A):

$$q_z=-\rho c_p\frac{\tau-0.5}{\tau}\sum_\alpha e_{\alpha z}f_\alpha \tag{8}$$

2.2. Multi-block LBM

In the present paper, we adopt a multi-block LBM for the heterogeneous computational domain in which the air gap in the contact region has physical properties different from other two blocks. One of the key issues of the multi-block LBM is the interface information exchange. A two-block system is shown in Fig. 2 to illustrate the basic idea of interfacial information exchange. The ratio of two lattice space is:

$$m=\delta x_c/\delta x_f=\delta t_c/\delta t_f \tag{9}$$

where subscript c and f represent the course grid and fine grid, respectively. The process of solving Eq. (3) can be divided into two steps: collision and streaming.

Collision step:

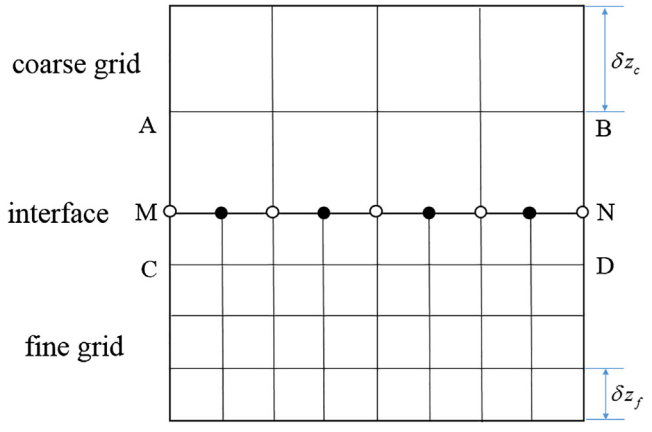

Fig. 2. Two-block grid system.

$$f_\alpha^+(\boldsymbol{x},t+\delta t)-f_\alpha(\boldsymbol{x},t)=-\frac{1}{\tau}[f_\alpha(\boldsymbol{x},t)-f_\alpha^{eq}(\boldsymbol{x},t)] \tag{10}$$

where f_α^+ is the post-collision temperature distribution function.

Steaming step:

$$f_\alpha(\boldsymbol{x}+\delta\boldsymbol{x},t+\delta t)=f_\alpha^+(\boldsymbol{x},t+\delta t) \tag{11}$$

To ensure the continuity of temperature and heat flux at the interface of two blocks, the temperature distribution function at the interface should be specially dealt with. The temperature distribution function can be divided into two parts, equilibrium part and non-equilibrium part:

$$f_\alpha(\boldsymbol{x},t)=f_\alpha^{eq}(\boldsymbol{x},t)+f_\alpha^{neq}(\boldsymbol{x},t) \tag{12}$$

Substituting Eq. (12) into Eq. (10) yields [24,26,33,34]:

$$f_\alpha^+(\boldsymbol{x},t+\delta t)=f_\alpha^{eq}(\boldsymbol{x},t)+\frac{\tau-1}{\tau}f_\alpha^{neq}(\boldsymbol{x},t) \tag{13}$$

Applying Eq. (13) for both coarse grid and fine grid systems yield [24,26,33,34]:

$$f_{\alpha,c}^+=f_{\alpha,c}^{eq}+\frac{\tau_c-1}{\tau_c}f_{\alpha,c}^{neq} \tag{14}$$

$$f_{\alpha,f}^+=f_{\alpha,f}^{eq}+\frac{\tau_c-1}{\tau_c}f_{\alpha,f}^{neq} \tag{15}$$

To ensure the continuity of the temperature at the interface, we should set [24,26,33,34]

$$f_{\alpha,c}^{eq}=f_{\alpha,f}^{eq} \tag{16}$$

To ensure the continuity of the heat flux at the interface, the following relation should be satisfied:

$$(\rho c_p)_f\frac{\tau_f-0.5}{\tau_f}\sum_\alpha e_{\alpha z}f_{\alpha,f}^{neq}=(\rho c_p)_c\frac{\tau_c-0.5}{\tau_c}\sum_\alpha e_{\alpha z}f_{\alpha,c}^{neq} \tag{17}$$

If we have the following relation:

$$f_{\alpha,f}^{neq}=\frac{(\rho c_p)_c}{(\rho c_p)_f}\frac{\tau_c-0.5}{\tau_f-0.5}\frac{\tau_f}{\tau_c}f_{\alpha,c}^{neq} \tag{18}$$

then the continuity of heat flux (Eq. (17)) can be ensured. In Eq. (18)

$$\frac{\tau_c-0.5}{\tau_f-0.5}=\frac{a_c}{a_f}\frac{\delta t_c}{\delta t_f}=m\frac{a_c}{a_f} \tag{19}$$

where a is the thermal diffusivity. Thus, it can be rewritten as:

$$f_{\alpha,f}^{neq}=\frac{(\rho c_p)_c}{(\rho c_p)_f}m\frac{a_c}{a_f}\frac{\tau_f}{\tau_c}f_{\alpha,c}^{neq}=m\frac{\lambda_c}{\lambda_f}\frac{\tau_f}{\tau_c}f_{\alpha,c}^{neq} \tag{20}$$

The expression that transforms the data from the coarse grid to the fine grid at the interface can be derived as follows:

$$\begin{aligned}f_{\alpha,c}^+&=f_{\alpha,c}^{eq}+\frac{\tau_c-1}{\tau_c}f_{\alpha,c}^{neq}=f_{\alpha,f}^{eq}+\frac{\tau_c-1}{\tau_c}\frac{\tau_c}{m\tau_f}\frac{\lambda_f}{\lambda_c}f_{\alpha,f}^{neq}\\&=f_{\alpha,f}^{eq}+\frac{\tau_c-1}{\tau_c}\frac{\tau_c}{m\tau_f}\frac{\lambda_f}{\lambda_c}(f_{\alpha,f}^+-f_{\alpha,f}^{eq})\frac{\tau_f}{\tau_f-1}=f_{\alpha,f}^{eq}+\frac{\tau_c-1}{\tau_f-1}\frac{\lambda_f}{m\lambda_c}(f_{\alpha,f}^+-f_{\alpha,f}^{eq})\end{aligned} \tag{21}$$

Similarly,

$$f_{\alpha,f}^+=f_{\alpha,c}^{eq}+m\frac{\tau_f-1}{\tau_c-1}\frac{\lambda_c}{\lambda_f}(f_{\alpha,c}^+-f_{\alpha,c}^{eq}) \tag{22}$$

The above equations can ensure the continuity of the heat flux at the interface.

The interface shown in Fig. 2 is shared by two regions. The unknown incoming temperature distribution functions at the interface are obtained from the neighboring blocks. For the D3Q7 LB model, $f_{5,c}^+(x,t)$ at the interface of the coarse block is obtained from $f_{5,f}^+(x,t)$ of the fine block, and $f_{6,f}^+(x,t)$ of the fine block is obtained from $f_{6,c}^+(x,t)$ of the

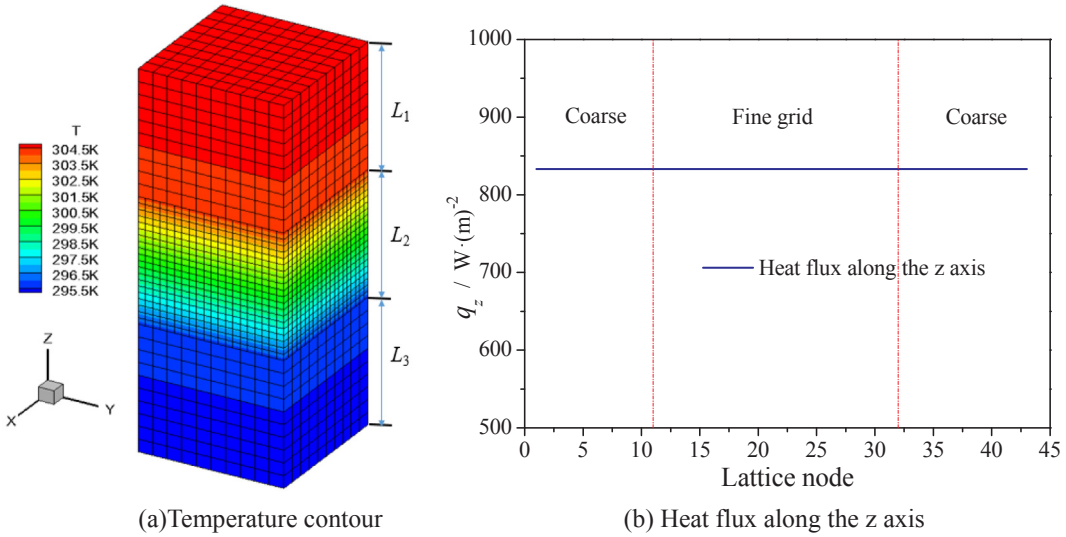

Fig. 3. Continuity of temperature and heat flux at the interfaces.

coarse block, according to Eqs. (21) and (22), respectively. However, there is no information at the nodes denoted by black symbols • if we want to obtain $f^{+}_{6,f}(x,t)$ from $f^{+}_{6,c}(x,t)$. Therefore, a cubic spline fitting is adopted for spatial interpolation on all the black-symbol nodes [24]:

$$f(x) = a_i + b_i x + c_i x^2 + d_i x^3, x_i \leqslant x \leqslant x_i, i = 1,2,\cdots,n \tag{23}$$

where the coefficients (a_i, b_i, c_i, d_i) are determined from the continuity conditions of the f,f',f'' at the nodes and suitable boundary conditions. Details can be found in Ref. [24].

The time matching step of the coarse grid and fine grid is quite different. If we want to obtain $f^{+}_{6,f}(x,t+\delta t_f)$, $f^{+}_{6,f}(x,t+2\delta t_f)$, $\cdots$, $f^{+}_{6,f}(x,t+(m-1)\delta t_f)$ from the data of the coarse grid, a temporal interpolation is needed. In the present paper, a three-point Lagrange interpolation is adopted [24]:

$$f(t) = \sum_{k=1}^{3} f(t_k)\left(\prod_{j=1,j\neq k} \frac{t-t_i}{t_k-t_j}\right) \tag{24}$$

The macroscopic temperature at the interface should be determined to obtain the equilibrium temperature distribution functions if we adopt Eqs. (21) and (22) to obtain the incoming temperature distribution functions. As shown in Fig. 2, the temperature of line $\overline{\mathrm{MN}}$ can be obtained by the interpolation of lines $\overline{\mathrm{AB}}$ and $\overline{\mathrm{CD}}$.

$$T_{\overline{\mathrm{MN}}} = \left(T_{\overline{\mathrm{MN}}} + m\frac{\lambda_f}{\lambda_c}T_{\overline{\mathrm{CD}}}\right) \Big/ \left(1 + m\frac{\lambda_f}{\lambda_c}\right) \tag{25}$$

2.3. Thermal contact resistance

As schematically shown in Fig. 1, the gaps in the contact region are filled with air or in vacuum. The thermal conductivity of the contact spot is much larger than that of the interstitial medium, resulting in a temperature drop at the contact interface. In the contact region, the heat flux transfers through the solid and interstitial medium (fluid). To ensure the continuity of the heat flux at the solid-fluid interface, we should put the interface at the middle of two nodes and assume that [35–37]:

$$(\rho c_p)_f = (\rho c_p)_s \tag{26}$$

where subscript f and s stand for the fluid and solid, respectively. It should be noted that this assumption will not influence the temperature field if the heat transfer reaches the steady state.

For the entire computational domain, the upper and bottom boundaries are assigned to be constant but at different temperatures. The other boundaries are assigned to be adiabatic. If the heat transfer reaches the steady state, the TCR of the contact surfaces can be calculated by the definition [38]:

$$R_c = \frac{\Delta t}{q} \tag{27}$$

where Δt is the temperature difference at the contact interface calculated by the upper surface and lower surface of the contact region, and q is the heat flux though the interface.

3. Validation

To validate the accuracy of the multi-block LBM developed in Sections 2.2 and 2.3, two benchmarks are presented in this section.

3.1. Three-component composite material

Similar to the layout of the Fig. 1, there are also three blocks in this case. Block 1 (top) and Block 3 (bottom) are coarse grids, while Block 2 (middle) is the fine grid. In this composite material, the thermal property of each block is homogeneous. The thermal conductivities of Block 1 and Block 3 are all 10 W/(m·K), and the thermal conductivity of Block 2 is 1 W/(m·K). The grid number of two coarse blocks are all $11 \times 11 \times 11$, and the grid number of the fine one is $21 \times 21 \times 21$. The length of each block is 1 cm, thus $L_1 = L_2 = L_3 = 1$ cm. The effective thermal conductivity of this composite material can be obtained by:

$$\frac{L_1 + L_2 + L_3}{\lambda_e} = \frac{L_1}{\lambda_1} + \frac{L_2}{\lambda_2} + \frac{L_3}{\lambda_3} \tag{28}$$

where λ_e is the effective thermal conductivity, and the theoretical result is 2.500 W/(m·K). For the simulation, the top surface is assigned to be 305 K; the bottom surface is assigned to be 295 K; and remained surfaces are adiabatic. The temperature contour and the heat flux along the z axis are shown in Fig. 3(a) and (b), respectively. It can be seen that the temperature and heat flux at the interface between neighbor blocks are continuous. The numerical prediction of the effective thermal conductivity of this composite material is 2.500 W/(m·K), which equals the theoretical results, validating the accuracy of the present method.

3.2. Simple model of thermal contact resistance

A simple model of two solids with imperfect surface sandwiched by a layer of air is used to mimic the TCR. As shown in Fig. 4(a), the distance of gap between two perfect surfaces is 5.2 μm, and the gap fills

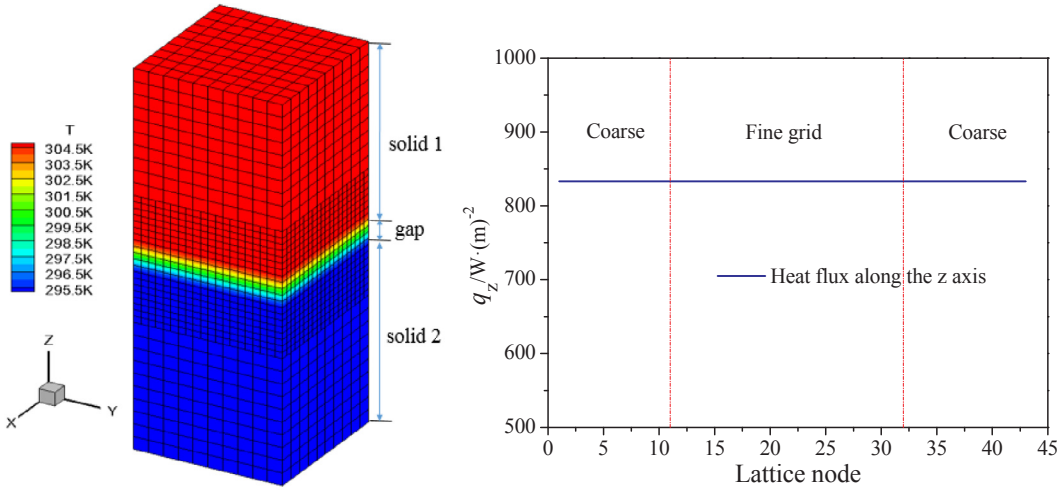

Fig. 4. A simple model of thermal contact resistance.

with air. The air thermal conductivity is 0.026 W/(m·K), and the thermal conductivities of the two solids are all 10 W/(m·K). The multi-block LBM is adopted to simulate this case. The boundary conditions are the same as those in Section 3.1. The results are shown in Fig. 4(b). It can be seen that the temperature and heat flux at the block-block interfaces and solid-air interfaces are all continuous. The numerical prediction of the TCR at the contact interface is 2×10^{-4} (m^2·K)/W, which is exactly the same as the theoretical result. The theoretical result of TCR of this case can be obtained by:

$$R_c = \frac{\delta}{\lambda_f} = \frac{5.2\ \mu\text{m}}{0.026\ \text{W/(m·K)}} = 2 \times 10^{-4}\ (\text{m}^2\text{·K})/\text{W} \tag{29}$$

where δ is the distance of gap, and λ_f is the thermal conductivity of the medium filling in the gap.

4. Results and discussions

4.1. The contact rough surface and contact pressure

In view of the self-affinity of the rough surface, a 3D fractal Weierstrass-Mandelbrot function is adopted to describe the real surface profile [5]:

$$z(x,y) = L\left(\frac{G}{L}\right)^{D-2}\left(\frac{\ln\gamma}{M}\right)^{1/2}\sum_{m=1}^{M}\sum_{n=0}^{n=n_{\max}}\gamma^{(D-3)n}\left\{\cos\phi_{m,n} - \cos\left[\frac{2\pi\gamma^n(x^2+y^2)^{1/2}}{L}\times\cos\left(\tan^{-1}\left(\frac{y}{x}\right) - \frac{\pi m}{M}\right) + \phi_{m,n}\right]\right\} \tag{30}$$

where D is the fractal dimension of the surface profile; G is the fractal roughness of the surface profile; L is the length of the sample; γ^n determines the frequency spectrum of surface roughness and $\gamma = 1.5$ is a typical value; n is the spatial frequency index, and its upper limit is given by $n_{\max} = \text{int}[\log(L/L_s)/\log\gamma]$, where L_s is the cut-off length at the order of atomic distance in materials; M is the number of the superposed ridges. Both the upper and lower surfaces are generated using Eq. (30) with $M = 10$, $n = 17$, $L = 8 \times 10^{-4}$ m, $G = 4 \times 10^{-10}$ m, $D = 2.40$ on three grid systems, $400(x) \times 400(y) \times 30(z)$, $800 \times 800 \times 30$ and $1600 \times 1600 \times 30$, respectively. After a preliminary test, the predicted TCR of $800 \times 800 \times 30$ is 15% higher than that of $400 \times 400 \times 30$, while 5% lower than that of $1600 \times 1600 \times 30$. As a compromise, all the results are based on the $800 \times 800 \times 30$ grid system for the contact region in the following study, and each grid represents 1 μm. The reconstructed contact rough surfaces based on the $800 \times 800 \times 30$ grid system are shown in Fig. 5. The root-mean-square roughness of the reconstructed surface is 1.938 μm. In Fig. 5, any node position (x, y, z) higher than the upper rough surface interface (calculated by Eq. (30)) is assigned as the solid node of material 1, while lower than the lower rough surface interface is assigned as the solid node of material 2. The void space between the upper and lower surface interfaces is assigned as the fluid node. The local solid-fluid interface is treated to be flat and is put right at the middle of two nodes. With the assumption of Eq. (26), the continuities of temperature and heat flux can be ensured at the solid-fluid interfaces. In the entire multi-block grid system, the ratio of two lattice space between the coarse grid and fine grid is eight, with a coarse grid of $100 \times 100 \times 100$ and a fine grid of $800 \times 800 \times 30$. This grid system is as a geometry input for the LB model. To speed up the calculation process, a parallel LBM code written in Fortran 90 using the OpenMP is developed.

Actually, when two rough surface are brought into contact, only a few contact spots exist, the contact stress is very large and the deformation tends to be plastic. On the other hand, the plastic model can be easily applied to obtain the contact pressure by counting the real contact area. Hence, the deformation of contact spots is assumed to be fully plastic in this study. The volume of deformed spot is assumed to be vanished automatically without changing the volumes of the neighbor spots [7]. The overall force balance yields the following relation [12]:

$$\frac{A_r}{A_a} = \frac{P}{H_c} \tag{31}$$

where A_r and A_a are the real area of contact spots and apparent areas (area of cross section), respectively; P is the contact pressure; H_c is the contact micro-hardness related to the deformation of the contact spot. The value of contact micro-hardness is 2.4 GPa for stainless steel joints while 0.927 GPa for aluminum joints [12]. In Fig. 5, A_r can be obtained by counting the node numbers of contact spots of two rough contact surface, while $A_a = 800 \times 800$, and thus the contact pressures of the two contact rough surfaces are 0.116 MPa and 5.179 MPa for Fig. 5(a) and (b), respectively.

4.2. The effect of the contact pressure

With the rough surface profile described in Section 4.1, we adopt the multi-block LBM presented in Section 2 to obtain the heat flux and the temperature drop at the interface and further to obtain the TCR of two contact solids. The temperature distribution contours of two contact stainless steels and the enlarged views of temperature contours of the local contact region (denoted in dashed frames) are shown in Fig. 6. The contact pressure is 0.4275 MPa for Fig. 6(a) while 40.16 MPa for

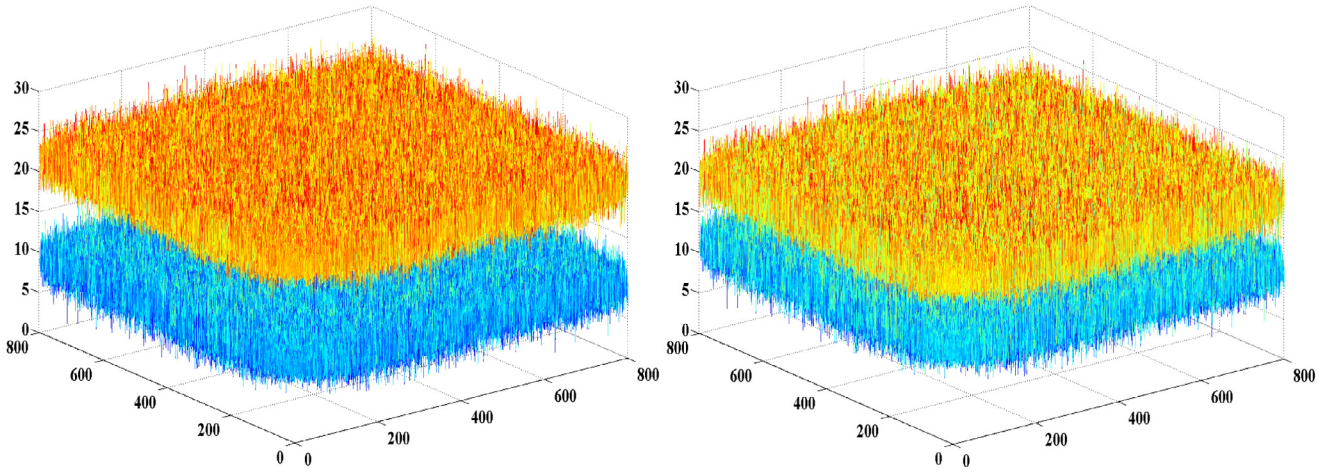

Fig. 5. Upper and lower rough surfaces at different loading contact pressures.

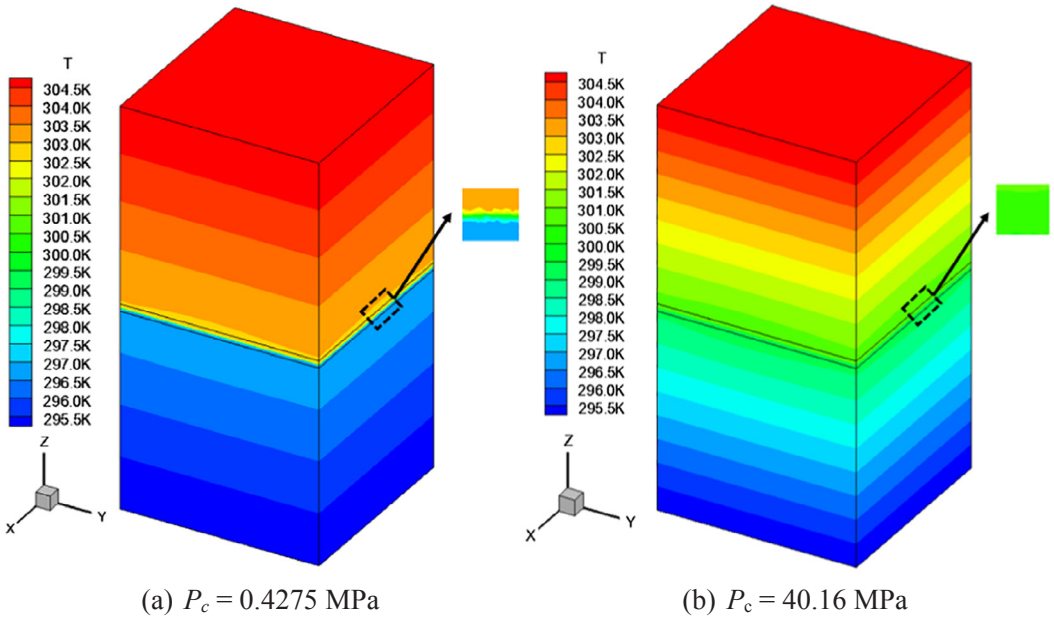

Fig. 6. Temperature contours at different loading contact pressures.

Fig. 6(b). It can be seen that the temperature drop at the interface of Fig. 6(a) is much larger than that of Fig. 6(b). The magnitude of temperature drop at the interface is proportional to the ratio of the TCR to the total thermal resistance since the total temperature difference of the entire domain is specified by the applied boundary conditions. The total thermal resistance is the summation of the TCR and thermal resistance of the bulk solid material. Thus, if the interfacial TCR is rather small compared to the thermal resistance of the bulk solid material, then the temperature drop at the interface is negligible. Otherwise, the interfacial TCR will cause a large temperature drop at the interface. A larger interfacial TCR will result in a larger temperature drop. In Fig. 6(b), the TCR at the loading contact pressure of 40.16 MPa is negligible since the temperature drop across the interface is rather small, while it will cause a significant temperature drop at the interface at the loading contact pressure of 0.4275 MPa.

The variation of the TCR with the loading contact pressure is shown in Fig. 7 for SS (stainless steel) vs. SS and Al (aluminum) vs. Al. It can be seen that the TCR first decreases rapidly and then more gently with the increase of pressure. The increasing loading contact pressure reduces

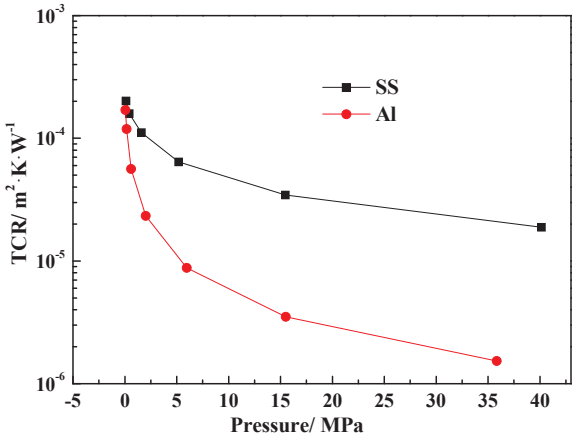

Fig. 7. Thermal contact resistance versus contact pressure.

the gap width between two rough surfaces. The thermal conductivity of the interstitial medium filling in the gap is much lower than that of the contact solids. Therefore, the reducing gap width leads to the decreasing in TCR. At the same loading contact pressure, the deformation of the contact aluminum is larger than that of the stainless steel due to the lower micro-hardness of aluminum. Thus, the interfacial TCR of two contact aluminums decreases faster than that of two contact stainless steels when the contact pressure increases. With further increase in the contact pressure, it becomes more and more difficult to further reduce the gap width. As a result, the decrease rate of the TCR becomes mild at a higher contact pressure.

4.3. The effect of the temperature and radiation

The thermal conductivities of the contact solids and interstitial medium (air) are all related to the temperature, and therefore the TCR is associated with the temperature. The variation of the TCR with the temperature from 300 K to 1000 K is shown in Fig. 8. It can be seen that the TCR decreases when the temperature increases. The interfacial TCR of two contact stainless steels is 1.59×10^{-4} m^2·K/W at 300 K while 6.72×10^{-5} m^2·K/W at 1000 K. At the contact region, both thermal conductivities of the contact solids and air increase with the temperature, making it easier to transfer heat across the interface. As a result, the interfacial TCR decreases with the increasing temperature.

The material radiant power increases with its temperature. To consider the effect of the radiation on the TCR, the upper surface of the contact region is assumed to be parallel to the lower surface. Then, the radiative heat transfer from the upper surface to the lower surface can be expressed as [39]:

$$q_r = \frac{5.67 \times 10^{-8} \times [T_{s1}^4 - T_{s2}^4]}{\frac{1}{\varepsilon_1} + \frac{1}{\varepsilon_2} - 1} \tag{32}$$

where T_{s1} is the average temperature of the upper surface; T_{s2} is the average temperature of the lower surface; ε_1 and ε_2 are the emissivity of the upper and lower surface, respectively. In the present paper, an additional heat source term is added at the nodes adjacent to the boundaries to consider the effect of radiation on the TCR. At the nodes adjacent to the boundaries of the upper surface, the additional heat source in Eq. (3) (or Eq. (1)) can be expressed as:

$$S = -\frac{q_r}{\delta z} \tag{33}$$

While at the nodes adjacent to the boundaries of the lower surface, the heat source in Eq. (3) (or Eq. (1)) can be expressed as:

$$S = \frac{q_r}{\delta z} \tag{34}$$

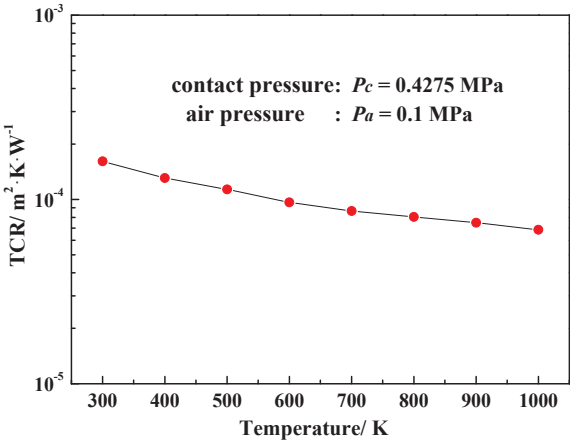

Fig. 8. Thermal contact resistance versus temperature.

where q_r is the radiative heat flux; δz is the grid space. At other nodes, the heat source is still zero. By converting the interfacial radiative heat flux into a volume-averaged source term of the nodes near-wall boundaries, we can simultaneously solve Eq. (3) at the entire computational domain to predict the TCR considering the effect of the radiation.

The radiative heat transfer adds a heat path at the contact region, and therefore will result in a smaller TCR. At the temperature of 1000 K and the contact pressure of 0.4275 MPa, the TCR is 6.72×10^{-5} m^2·K/W for the case considering the radiation while 6.84×10^{-5} m^2·K/W without considering the radiation when the air thermal conductivity is 6.63×10^{-2} W/(m·K). It means that the contribution of radiative heat flux to the total heat flux is only 1.79%. It makes not much difference if we neglected the contribution of the radiation to the TCR. However, if the air thermal conductivity is 6.63×10^{-4} W/(m·K), the TCR is 2.48×10^{-3} m^2·K/W for the case considering the radiation while 3.97×10^{-3} m^2·K/W without considering the radiation at the temperature of 1000 K. The radiation plays a significant role in predicting the TCR at a high temperature if the air thermal conductivity is close to zero or even the gap is in vacuum. At this situation, we cannot neglect the effect of the radiation to the TCR.

4.4. The effect of thermal conductivities of the contact solids and interstitial medium

As indicated above, three paths for the heat to across the contact region are: (i) conduction of the contact spots; (ii) conduction of air filling in gaps; (iii) radiation. Therefore, thermal conductivities of the contact materials and interstitial medium will influence the value of the TCR. At 300 K, their effects on the TCR are shown in Fig. 9. The TCR at the thermal conductivity of the interstitial medium being 2.6×10^{-4} W/(m·K) is approximately 50 times of that at the thermal conductivity of the interstitial medium being 2.6×10^{-2} W/(m·K) at the low contact pressure. Due to the fact that only few contact spots exist at the low contact pressure, the gas conduction is the only major heat transfer path across the interface. Therefore, the thermal conductivity of the interstitial medium plays a significant role in the TCR, especially at a low contact pressure. Fig. 10(a) and (b) show temperature distribution contours with thermal conductivities of interstitial medium being 2.6×10^{-4} W/(m·K) and 2.6×10^{-2} W/(m·K), respectively, at a low loading contact pressure of 0.4275 MPa. It can be seen that the temperature drop at the interface in Fig. 10(a) is much larger than that in Fig. 10(b), and almost the entire temperature difference drops on the interface for Fig. 10(a). As discussed in Section 4.2, the temperature drop at the interface is proportional to the ratio of interfacial TCR to the total thermal resistance when the temperature

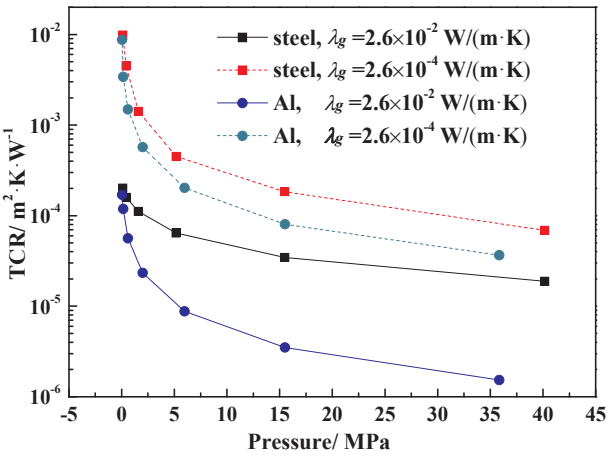

Fig. 9. Effect of thermal conductivities of contact solids and interstitial medium on thermal contact resistance.

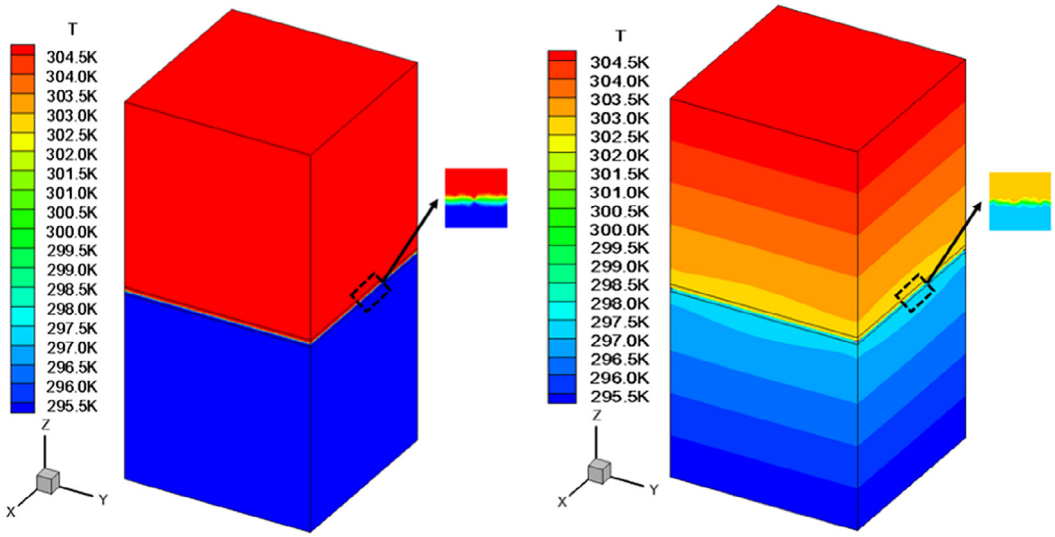

(a) $\lambda_g = 2.6\times10^{-4}$ W/(m·K) (b) $\lambda_g = 2.6\times10^{-2}$ W/(m·K)

Fig. 10. Temperature distribution contours at different thermal conductivities of interstitial media.

difference of the entire domain is given. At a low loading contact pressure of 0.4275 MPa and thermal conductivities of interstitial medium being 2.6×10^{-4} W/(m·K), the interfacial TCR is dominant in the total thermal resistance, resulting in a such large temperature drop at the interface for Fig. 10(a).

From Fig. 9, we can also find that the interfacial TCR of two contact aluminums is smaller than that of stainless steels, and such difference becomes smaller at the low contact pressure since the contribution of the gas conduction is a dominant factor for the TCR at the low contact pressure. The thermal conductivity of the contact spots cannot affect the TCR much due to the few contact spots at the low contact pressure. At a higher contact pressure, such difference becomes significant since contact spot numbers increase with the contact pressure, making the thermal conductivity of contact spots to be a significant factor for the TCR.

4.5. The effect of the roughness

The surface profiles of two contact surfaces will have an influence on the TCR, especially the root-mean-square roughness of the surface profiles. We reconstructed the rough surfaces based on the fractal theory with different root-mean-square roughness (*Ra*) varying from 0.951 μm to 5.705 μm. The variation of TCR with the root-mean-square roughness of the rough surface is shown in Fig. 11. It can be seen that the TCR increases with the root-mean-square roughness. The increasing root-mean-square roughness enlarges the distance between the upper and lower surface, resulting in the increase of the TCR.

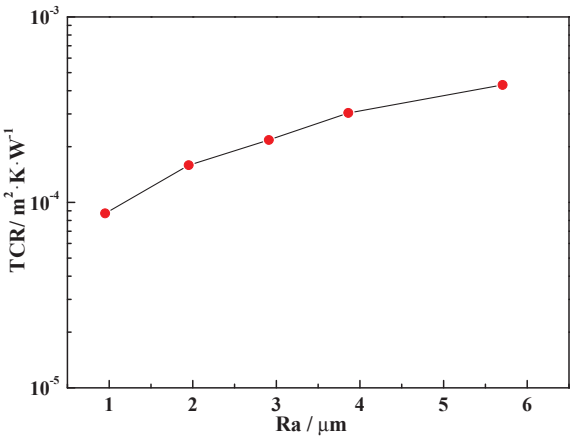

Fig. 11. Effect of surface roughness on thermal contact resistance.

5. Conclusion

In the present paper, a patching type multi-block parallel lattice Boltzmann method based on the OpenMP is adopted to predict the TCR at the interface of two solids. The rough surface of the contact solids is described based on the fractal theory. After validations, the effects of the contact pressure, roughness, temperature, radiation, solid and gas thermal conductivities, on the TCR are investigated. Conclusions can be drawn as follows:

(1) The TCR decreases when the loading contact pressure increases, while increases with the root-mean-square roughness; the interfacial TCR of two contact aluminums decreases faster than that of two contact stainless steels when the contact pressure increases;
(2) The influence of temperature on the TCR comes from the temperature-dependent thermal conductivity. At the high temperature, the contribution of the radiation to the TCR becomes appreciable if the thermal conductivity of the interstitial medium is low. Especially when the gap is in vacuum, the radiation contribution on the TCR cannot be neglected.
(3) The thermal conductivity of interstitial medium plays a significant role in predicting TCR, especially at a low contact pressure. When the thermal conductivity of interstitial medium is close to zero or the gap is in vacuum, the TCR is much larger than that filled with air.

Acknowledgement

This study is supported by the Key Project of International Joint Research of National Natural Science Foundation of China (51320105004) and 111 Project (B16038).

Appendix A. Chapman-Enskog expansion

Eq. (3) can be expanded using the Tylor series:

$$D_\alpha f_\alpha + \frac{\delta t}{2} D_\alpha^2 f_\alpha = -\frac{1}{\tau \delta t}(f_\alpha - f_\alpha^{\mathrm{eq}}) \tag{A.1}$$

where

$$D_\alpha = \frac{\partial}{\partial t} + \boldsymbol{e}_\alpha \cdot \nabla \tag{A.2}$$

According to the idea of the Chapman-Enskog expansion, we have [24]

$$f_\alpha = f_\alpha^{(0)} + \epsilon f_\alpha^{(1)} + \epsilon^2 f_\alpha^{(2)} + \ldots \tag{A.3}$$

$$\partial_{x_i} = \epsilon \, \partial_{x_i} \tag{A.4}$$

$$\partial_t = \epsilon^2 \, \partial_t \tag{A.5}$$

where $f_\alpha^{(0)}$ is $f_\alpha^{(eq)}$. From Eq. (7) and (A.3), we can obtain:

$$\sum_\alpha f_\alpha^{(1)} = 0 , \sum_\alpha f_\alpha^{(2)} = 0 \tag{A.6}$$

According to the definition of the discrete velocity, we have

$$\sum_\alpha e_{\alpha i} \omega_\alpha = 0 \tag{A.7}$$

$$\sum_\alpha e_{\alpha i} e_{\alpha j} \omega_\alpha = \varepsilon c^2 \delta_{ij} \tag{A.8}$$

$$\sum_\alpha e_{\alpha i} e_{\alpha j} e_{\alpha k} \omega_\alpha = 0 \tag{A.9}$$

In the present D3Q7 model, $\varepsilon = 2/7$. Substituting Eqs. ((A.3)-(A.5)) into Eq. (A.1) and then equating the coefficients of the same order yield the following relations:

$$\epsilon^1 : e_{\alpha_i} \frac{\partial f_\alpha^{(0)}}{\partial x_i} = -\frac{1}{\tau \delta t} f_\alpha^{(1)} \tag{A.10}$$

$$\epsilon^2 : \frac{\partial f_\alpha^{(0)}}{\partial t} + e_{\alpha_i} \frac{\partial f_\alpha^{(1)}}{\partial x_i} + \frac{\delta t}{2} e_{\alpha i} e_{\alpha j} \frac{\partial^2 f_\alpha^{(0)}}{\partial x_i \partial x_j} = -\frac{1}{\tau \delta t} f_\alpha^{(2)} \tag{A.11}$$

Multiplying Eq. (A.10) by $e_{\alpha z}$ and then summing all the directions give:

$$\sum_\alpha e_{\alpha z} \, e_{\alpha i} \frac{\partial f_\alpha^{(0)}}{\partial x_i} = -\frac{1}{\tau \delta t} \sum_\alpha e_{\alpha z} f_\alpha^{(1)} \tag{A.12}$$

For the left hand side of the Eq. (A.12), we have

$$\sum_\alpha e_{\alpha z} \, e_{\alpha i} \frac{\partial f_\alpha^{(0)}}{\partial x_i} = \sum_\alpha e_{\alpha z} \, e_{\alpha i} \omega_\alpha \frac{\partial T}{\partial x_i} = \varepsilon c^2 \delta_{iz} \frac{\partial T}{\partial x_i} = \varepsilon c^2 \frac{\partial T}{\partial z} \tag{A.13}$$

Therefore, we can obtain

$$\varepsilon c^2 \frac{\partial T}{\partial z} = -\frac{1}{\tau \delta t} \sum_\alpha e_{\alpha z} f_\alpha^{(1)} \tag{A.14}$$

Differentiating Eq. (A.10) gives:

$$\frac{\partial f_\alpha^{(1)}}{\partial x_i} = -e_{\alpha j} \frac{\partial^2 f_\alpha^{(0)}}{\partial x_i \partial x_j} \tau \delta t \tag{A.15}$$

Rewrite the left hand side of Eq. (A.11) as follows:

$$\frac{\partial f_\alpha^{(0)}}{\partial t} + e_{\alpha i} \frac{\partial f_\alpha^{(1)}}{\partial x_i} + \frac{\delta t}{2} e_{\alpha i} e_{\alpha j} \frac{\partial^2 f_\alpha^{(0)}}{\partial x_i \partial x_j} = \frac{\partial f_\alpha^{(0)}}{\partial t} - e_{\alpha i} \, e_{\alpha j} \frac{\partial f_\alpha^{(0)}}{\partial x_i \partial x_j} \tau \delta t + \frac{\delta t}{2} e_{\alpha i} e_{\alpha j} \frac{\partial^2 f_\alpha^{(0)}}{\partial x_i \partial x_j} = \frac{\partial f_\alpha^{(0)}}{\partial t} + \tau \delta t \left(\frac{1}{2\tau} - 1 \right) e_{\alpha i} e_{\alpha j} \frac{\partial^2 f_\alpha^{(0)}}{\partial x_i \partial x_j} \tag{A.16}$$

The summation of Eq. (A.11) over all the directions gives:

$$\frac{\partial \sum_{\alpha=0}^{n} f_\alpha^{(0)}}{\partial t} + \tau \delta t \left(\frac{1}{2\tau} - 1 \right) \sum_{\alpha=0}^{n} e_{\alpha i} e_{\alpha j} \frac{\partial^2 f_\alpha^{(0)}}{\partial x_i \partial x_j} = \frac{\partial T}{\partial t} - \tau \delta t \left(1 - \frac{1}{2\tau} \right) \varepsilon c^2 \delta_{ij} \frac{\partial^2 T}{\partial x_i \partial x_j} = \frac{\partial T}{\partial t} - \tau \delta t \left(1 - \frac{1}{2\tau} \right) \varepsilon c^2 \frac{\partial^2 T}{\partial^2 x_i} = 0 \tag{A.17}$$

Compared with the macroscopic energy diffusion equation, we obtain:

$$D = \varepsilon c^2\left(\tau-\frac{1}{2}\right)\delta t = \frac{2}{7}c^2(\tau-\frac{1}{2})\delta t \tag{A.18}$$

Multiplying Eq. (A.11) by $e_{\alpha z}$ and then summing all the directions give:

$$\frac{\partial \sum_\alpha e_{\alpha z} f_\alpha^{(0)}}{\partial t} + \tau\delta t\left(\frac{1}{2\tau}-1\right)\sum_\alpha e_{\alpha z}e_{\alpha i}e_{\alpha j}\frac{\partial^2 f_\alpha^{(0)}}{\partial x_i \partial x_j} = -\frac{1}{\tau\delta t}\sum_\alpha e_{\alpha z} f_\alpha^{(2)} \tag{A.19}$$

According to the definitions of the equilibrium distribution function and Eqs. ((A.7)-(A.9)), we have:

$$\sum_\alpha e_{\alpha z} f_\alpha^{(0)} = 0 \tag{A.20}$$

$$\sum_\alpha e_{\alpha z}e_{\alpha i}e_{\alpha j}\frac{\partial^2 f_\alpha^{(0)}}{\partial x_i \partial x_j} = 0 \tag{A.21}$$

Therefore, Eq. (A.19) becomes:

$$-\frac{1}{\tau\delta t}\sum_\alpha e_{\alpha z} f_\alpha^{(2)} = 0 \tag{A.22}$$

Combining Eq. (A.14), (A.20) and (A.22), we can obtain:

$$\varepsilon c^2\frac{\partial T}{\partial z} = -\frac{1}{\tau\delta t}\sum_\alpha e_{\alpha z} f_\alpha \tag{A.23}$$

Therefore, the local heat flux can be obtained by:

$$q = \lambda\frac{\partial T}{\partial z} = -\rho c_p\frac{\tau-0.5}{\tau}\sum_\alpha e_{\alpha z} f_\alpha \tag{A.24}$$

Appendix B. Supplementary material

Supplementary data associated with this article can be found, in the online version, at http://dx.doi.org/10.1016/j.applthermaleng.2018.03.095.

References

[1] M.G. Cooper, B.B. Mikic, M.M. Yovanovich, Thermal contact conductance [J], Int. J. Heat Mass Transf. 12 (3) (1969) 279–300.
[2] M. Zou, B. Yu, J. Cai, et al., Fractal model for thermal contact conductance [J], ASME J. Heat Transf. 130 (10) (2008) 101301.
[3] X. Miao, X. Huang, A complete contact model of a fractal rough surface [J], Wear 309 (1) (2014) 146–151.
[4] R.L. Jackson, S.H. Bhavnani, T.P. Ferguson, A multiscale model of thermal contact resistance between rough surfaces [J], ASME J. Heat Transf. 130 (8) (2008) 081301.
[5] M.V. Murashov, S.D. Panin, Numerical modelling of contact heat transfer problem with work hardened rough surfaces[J], Int. J. Heat Mass Transf. 90 (2015) 72–80.
[6] J.J. Gou, X.J. Ren, Y.J. Dai, et al., Study of thermal contact resistance of rough surfaces based on the practical topography[J], Comput. Fluids (2016).
[7] S.M.S. Wahid, Numerical analysis of heat flow in contact heat transfer [J], Int. J. Heat Mass Transf. 46 (24) (2003) 4751–4754.
[8] T. Cui, Q. Li, Y. Xuan, et al., Multiscale simulation of thermal contact resistance in electronic packaging[J], Int. J. Therm. Sci. 83 (2014) 16–24.
[9] P. Zhang, Y.M. Xuan, Q. Li, A high-precision instrumentation of measuring thermal contact resistance using reversible heat flux [J], Exp. Therm Fluid Sci. 54 (2014) 204–211.
[10] J. Hong, J. Peng, B. Li, An integrated mechanical–thermal predictive model of thermal contact conductance [J], ASME J. Heat Transf. 135 (4) (2013) 041301.
[11] J.A. Greenwood, J.B.P. Williamson, Contact of nominally flat surfaces[C], Proc. Royal Soc. London A: Math., Phys. and Eng. Sci., 295(1442) (1966) 300–319.
[12] M.M. Yovanovich, Four decades of research on thermal contact, gap, and joint resistance in microelectronics [J], IEEE Trans. Compon. Packag. Technol. 28 (2) (2005) 182–206.
[13] R.S. Sayles, T.R. Thomas, Surface topography as a nonstationary random process [J], Nature 271 (5644) (1978) 431–434.
[14] A. Majumdar, C.L. Tien, Fractal characterization and simulation of rough surfaces [J], Wear 136 (2) (1990) 313–327.
[15] X. Zhang, P. Cong, S. Fujiwara, et al., A new method for numerical simulation of thermal contact resistance in cylindrical coordinates [J], Int. J. Heat Mass Transf. 47 (5) (2004) 1091–1098.
[16] P.R. Nayak, Random process model of rough surfaces in plastic contact [J], Wear 26 (3) (1973) 305–333.
[17] B.B. Mikić, Thermal contact conductance: theoretical considerations [J], Int. J. Heat Mass Transf. 17 (2) (1974) 205–214.
[18] L. Kogut, I. Etsion, Elastic-plastic contact analysis of a sphere and a rigid flat [J], J. Appl. Mech. 69 (5) (2002) 657–662.
[19] J. Tang, A.K. Tieu, Z.Y. Jiang, Modelling of oxide scale surface roughness in hot metal forming [J], J. Mater. Process. Technol. 177 (1) (2006) 126–129.
[20] M.M. Yovanovich, W.W. Kitscha, Modeling the effect of air and oil upon the thermal resistance of a sphere-flat contact[C], in: American Institute of Aeronautics and Astronautics, Thermophysics Conference, 8th, Palm Springs, Calif, Research supported by the National Research Council of Canada, vol. 16, no. 18, 1973.
[21] W.Q. Tao, Advances in Computational Heat Transfer [M], Science Press, Beijing, 2001 Chapter 2.
[22] P. Heino, Multiscale lattice Boltzmann finite difference model for thermal conduction from nanoscale hot spots [J], Int. J. Multiscale Computat. Eng. 6 (2) (2008) 169–178.
[23] A. Christensen, S. Graham, Multiscale lattice Boltzmann modeling of phonon transport in crystalline semiconductor materials [J], Numer. Heat Transf., Part B: Fundam. 57 (2) (2010) 89–109.
[24] D. Yu, R. Mei, W. Shyy, A multi-block lattice Boltzmann method for viscous fluid flows [J], Int. J. Numer. Meth. Fluids 39 (2) (2002) 99–120.
[25] S. Chen, G.D. Doolen, Lattice Boltzmann method for fluid flows [J], Annu. Rev. Fluid Mech. 30 (1) (1998) 329–364.
[26] Y.L. He, Y. Wang, Q. Li, Lattice Boltzmann Method: Theory and Applications [M], Science Press, Beijing, 2009.
[27] L. Chen, Q. Kang, Y.L. He, et al., Pore-scale simulation of coupled multiple physicochemical thermal processes in micro reactor for hydrogen production using lattice Boltzmann method [J], Int. J. Hydrogen Energy 37 (19) (2012) 13943–13957.
[28] M. Wang, N. Pan, Modeling and prediction of the effective thermal conductivity of random open-cell porous foams [J], Int. J. Heat Mass Transf. 51 (5) (2008) 1325–1331.
[29] M. Hussain, E. Tian, T.F. Cao, et al., Pore scale modeling of effective diffusion coefficient of building materials, Int. J. Heat Mass Transf. 90 (2015) 1266–1274.
[30] M. Hermanns, Parallel Programming in Fortran 95 using OpenMP [J], Universidad Politecnica de Madrid, Spain, 2002.
[31] S.C. Mishra, H. Poonia, R.R. Vernekar, et al., Lattice Boltzmann method applied to radiative transport analysis in a planar participating medium[J], Heat Transf. Eng. 35 (14–15) (2014) 1267–1278.
[32] W.Z. Fang, J.J. Gou, H. Zhang, et al., Numerical predictions of the effective thermal conductivity for needled C/C-SiC composite materials, Numer. Heat Transf. Part A: Appl. 70 (10) (2016) 1101–1117.
[33] D. Yu, R. Mei, L.S. Luo, et al., Viscous flow computations with the method of lattice Boltzmann equation [J], Prog. Aerosp. Sci. 39 (5) (2003) 329–367.
[34] D. Yu, S.S. Girimaji, Multi-block lattice Boltzmann method: extension to 3D and validation in turbulence [J], Phys. A: Statist. Mech. Appl. 362 (1) (2006) 118–124.
[35] M. Wang, J. Wang, N. Pan, et al., Mesoscopic predictions of the effective thermal conductivity for microscale random porous media[J], Phys. Rev. E 75 (3) (2007) 036702.

[36] W.Z. Fang, L. Chen, J.J. Gou, et al., Predictions of effective thermal conductivities for three-dimensional four-directional braided composites using the lattice Boltzmann method[J], Int. J. Heat Mass Transf. 92 (2016) 120–130.
[37] W.Z. Fang, H. Zhang, L. Chen, et al., Numerical predictions of thermal conductivities for the silica aerogel and its composites[J], Appl. Therm. Eng. 115 (2017) 1277–1286.
[38] C.V. Madhusudana, C.V. Madhusudana, Thermal Contact Conductance [M], Springer-Verlag, New York, 1996.
[39] M.F. Modest, Radiative Heat Transfer [M], Academic Press, 2013.